MOX-Report No. 29/2021

Image-based computational hemodynamics analysis of systolic obstruction in hypertrophic cardiomyopathy

Fumagalli, I.; Vitullo, P.; Vergara, C.; Fedele, M.; Corno, A.F.; Ippolito, S.; Scrofani, R.; Quarteroni, A.

MOX, Dipartimento di Matematica
Politecnico di Milano, Via Bonardi 9 - 20133 Milano (Italy)

mox-dmat@polimi.it http://mox.polimi.it

Image-based computational hemodynamics analysis of systolic obstruction in hypertrophic cardiomyopathy

Ivan Fumagalli[1*], Piermario Vitullo[1], Christian Vergara[2], Marco Fedele[1], Antonio F. Corno[3], Sonia Ippolito[4], Roberto Scrofani[5], Alfio Quarteroni[1,6]

[1]MOX, Dipartimento di Matematica, Politecnico di Milano, Milan, Italy

[2]LaBS - Dipartimento di Chimica, Materiali e Ingegneria Chimica "Giulio Natta", Politecnico di Milano, Milan, Italy

[3]Children's Heart Institute, Hermann Children's Hospital, University of Texas Health, McGovern Medical School, Houston, TX, United States of America

[4]Radiology Unit, L. Sacco Hospital, Milan, Italy

[5]Cardiac Surgery Unit, L. Sacco Hospital, Milan, Italy

[6]Institute of Mathematics, École Polytechnique Fédérale de Lausanne, Lausanne, Switzerland

*** Correspondence:**
Ivan Fumagalli
ivan.fumagalli@polimi.it

Keywords: hypertrophic cardiomyopathy, septal myectomy, cardiac cine-MRI, image-based computational fluid dynamics, mitral valve, patient-specific simulations

Abstract

Hypertrophic Cardiomyopathy (HCM) is a pathological condition characterized by an abnormal thickening of the myocardium. When affecting the medio-basal portion of the septum, it is named Hypertrophic Obstructive Cardiomyopathy (HOCM) because it induces a flow obstruction in the left ventricular outflow tract. In any type of HCM, the myocardial function can become compromised, possibly resulting in cardiac death. In this study, we investigated with computational analysis the hemodynamics of patients with different types of HCM. The aim was quantifying the effects of this pathology on the intraventricular blood flow and pressure gradients, and providing information potentially useful to guide the indication and the modality of the surgical treatment (septal myectomy). We employed an image-based computational approach, integrating fluid dynamics simulations with geometrical and functional data, reconstructed from standard cardiac cine-MRI acquisitions. We showed that with our approach we can better understand the patho-physiological behavior of intraventricular blood flow dynamics due to the abnormal morphological and functional aspect of the left ventricle. The main results of our investigation are: a) a detailed patient-specific analysis of the blood velocity, pressure and stress distribution associated to HCM; b) clinical guidelines for patients affected by HOCM, dictated by their computational-based classification.

1 Introduction

Hypertrophic Cardiomyopathy (HCM) is a typically congenital cardiac disorder characterized by an abnormal thickening of the myocardium (wall thickness exceeding 15 mm, in adult patients) without additional causes inducing secondary hypertrophy [Elliott et al. 2014]. The prevalence is 0.2–0.6% in the Western world population, with a reported annual mortality rate of 1%. When the thickening affects the medio-basal region of the interventricular septum, this condition may cause a flow obstruction in the Left Ventricular Outflow Tract (LVOT), and thus it is named Hypertrophic Obstructive Cardiomyopathy (HOCM). People with mild forms of HOCM often remain oligosymptomatic or even asymptomatic for many years. Otherwise, they may develop dyspnea, angina pectoris, or stress-induced syncope, with an increased risk of sudden cardiac death, particularly in young people and athletes, more easily exposed to physical efforts that require a sudden increase of the cardiac output. The pathological effects of HOCM can be worsened by concurrent conditions increasing the ventricular pressure afterload, such as systemic hypertension and/or aortic valve stenosis. The LVOT obstruction is dynamical, and largely influenced by changes in left ventricular pressure overload and contractility, with subsequently increased systolic pressure in the Left Ventricle (LV) and possible secondary Mitral Valve Regurgitation (MVR), myocardial ischemia, and reduction in cardiac output. In particularly severe conditions, a Systolic Anterior Motion (SAM) of the mitral valve can occur, thus further worsening the LVOT obstruction [Sherrid et al. 2016, Akiyama et al. 2017, Geske et al. 2012, Ibrahim et al. 2012, Jiang et al. 1987].

One of the most frequently employed surgical treatments for a pathologically relevant HOCM is the septal myectomy, namely the resection of a portion of the interventricular septum, to abolish or reduce the obstruction in the LVOT [Elliott et al. 2014, Nicolò et al. 2019, Ommen et al. 2005, Maron et al. 2014, Morrow et al. 1975]. Therefore, identifying the location and extension of the septal region responsible for such obstruction is of paramount importance to guide the preoperative design of the surgical procedure.

To obtain quantitative indications on velocity patterns, pressure gradients and wall shear stresses associated to the ventricular blood flow dynamics, computational hemodynamics approaches have proved to be extremely helpful, thanks to their flexibility and level of detail [Quarteroni et al. 2017]. In this regard, two main standpoints are currently adopted: Fluid-Structure Interaction (FSI) simulations and prescribed-motion Computational Fluid Dynamics (CFD). The first approach consists in looking for the coupled solution of the fluid dynamics of blood flow and of the structure mechanics of the myocardium and cardiac valves, thus requiring a proper calibration of the mechanical parameters of the tissue, and possibly entailing a very high computational cost [Kunzelman et al. 2007, Su et al. 2014, Lassila et al. 2017, Feng et al. 2019, Collia et al. 2019, Kaiser et al. 2019, Meschini et al. 2021, Gao et al. 2017, Karabelas et al. 2018]. On the other hand, in image-based CFD, the patient-specific displacement of the myocardium and valves leaflets is reconstructed from kinetic medical images (such as cardiac cine-MRI) and then prescribed as endocardial displacement to obtain the fluid domain configuration. This latter approach, by reducing the mathematical complexity of the problem with respect to a full FSI system, at the expense of requiring a more complex image processing procedure, has provided insightful indications on cardiovascular diseases in a series of reports [Su et al. 2016, D'Elia et al. 2011, This et al. 2020, Otani et al. 2016, Chnafa et al. 2016, Seo et al. 2014, Bavo et al. 2017], including the computational study of HCM [Deng et al. 2018, Nardi et al. 2019, Fumagalli et al. 2020]. In all the quoted references, the reconstruction of the endocardium geometry was mainly based on the sole short-axis acquisition series, whereas long-axis views are only employed to identify some specific points or distances. This limitation was mainly due to the relative difficulty of combining the data from

different acquisitions. By the improved reconstruction procedure that we propose and employ in the present study, we merge all the cine-MRI series in a single image, thus extracting all the geometrical information from images and yielding an improved accuracy on the computational domain.

The goal of this study was to investigate the hemodynamics in the systolic phase and the LVOT obstruction severity and extent in patients with HCM, and also to provide quantitative information useful to potentially guide the design of the possible surgical treatment. We used the computational procedure [Fumagalli et al. 2020], based on cardiac cine-MRI data, and we introduced further improvements based on the integration of short-axis and long-axis views, to accurately reconstruct the patient-specific geometry and motion of the LV and of the ascending aorta, and to set up the conditions for a CFD analysis. This motion was then extended to the mitral valve leaflets, whose effects on the hemodynamics were accounted for by a resistive method [Fumagalli et al. 2020, Fedele et al. 2017].

The novelty of this study consists in the quantitative comparison of patients with some types of HCM by means of the extended computational procedure outlined above, based on routinely acquired cardiac cine-MRI data. This results in a CFD-based assessment and classification of the severity of the HCM-induced flow obstruction with ad-hoc designed hemodynamical indicators, and the identification of the region of the septal wall most suitable for the surgical approach by septal myectomy. The systematic discussion of the outcomes represents a step forward towards the applicability of our computational tools to accompany standard diagnostical procedures, and the definition of a comprehensive severity score for HOCM including hemodynamics indicators.

2 Methods

In the present section, we describe the imaging data on which this study is based, and we introduce a computational procedure encompassing image processing, surface morphing, and numerical simulations for the study of the hemodynamics in LV and ascending aorta.

2.1 Patients data

Cardiac cine-MRI data of three patients were provided by L. Sacco Hospital in Milano, Italy, with the approval of the Ethics Committee and in accordance with the ethics guideline of the institutions involved, including the signed consent of the patient. The main characteristics of the patients are reported in Table 1.

Table 1 - Main characteristics of the HCM patients investigated.

Patient	**1**	**2**	**3**
Age	57	66	83
Sex	F	M	F
EDWM [g]	240	216	98
Max IV septum thickness [mm]	25	18	16
Right ventricle free wall	hypertrophic	regular	regular
MV regurgitation	NO	NO	NO
Description of LV hypertrophy	concentric, symmetric HCM, amyloidosis infiltrations	concentric HCM, distributed hypokinesis	symmetric HCM, preserved global systolic function

The following are the clinical features of the patients:

- Patient 1. The overall contractility of the right ventricle is preserved, despite the hypertrophy involving also the free right ventricular wall, and in contrast with the reduced overall systolic function of the LV. She also presented with a mild pericardial effusion. No valves regurgitation or stenosis were reported.
- Patient 2. This patient is a smoker, hypertensive and overweight; he experienced chest pain and incipient dyspnea, and was recently hospitalized for heart failure. Subsequent electrocardiography limited the electrophysiological findings to sporadic extrasystoles. A trivial degree of regurgitation was reported for the aortic and tricuspid valves, but note for the mitral valve. The right ventricle had a significantly reduced systolic function (ejection fraction = 12%) although the values of its walls thickness remained in the normal range.
- Patient 3. No effusions, edemas, fibrosis, or other concurrent conditions were reported, except for a prolapse of the anterior leaflet of the mitral valve towards the septum (SAM), without regurgitation.

For each patient, the data included different views, with different resolution properties: a volumetric short-axis acquisition, with a spacing and a slice thickness of 8mm along the LV main axis, a space resolution of 1mm and a time resolution of 1/20 of the heartbeat; a set of single-slice, two-dimensional long-axis acquisitions on the so-called two-chambers, three-chambers, and four-chambers planes, with space resolution of 1mm and time resolution of 1/20 or 1/30 of the heartbeat. These are standard cardiac cine-MRI data, routinely acquired during diagnostical procedures: the reconstruction algorithm presented in this study does not require the setup of ad-hoc acquisitions.

So far, none of these patients underwent surgery yet, based on the indications given by their attending clinicians.

2.2 Reconstruction of geometry and motion

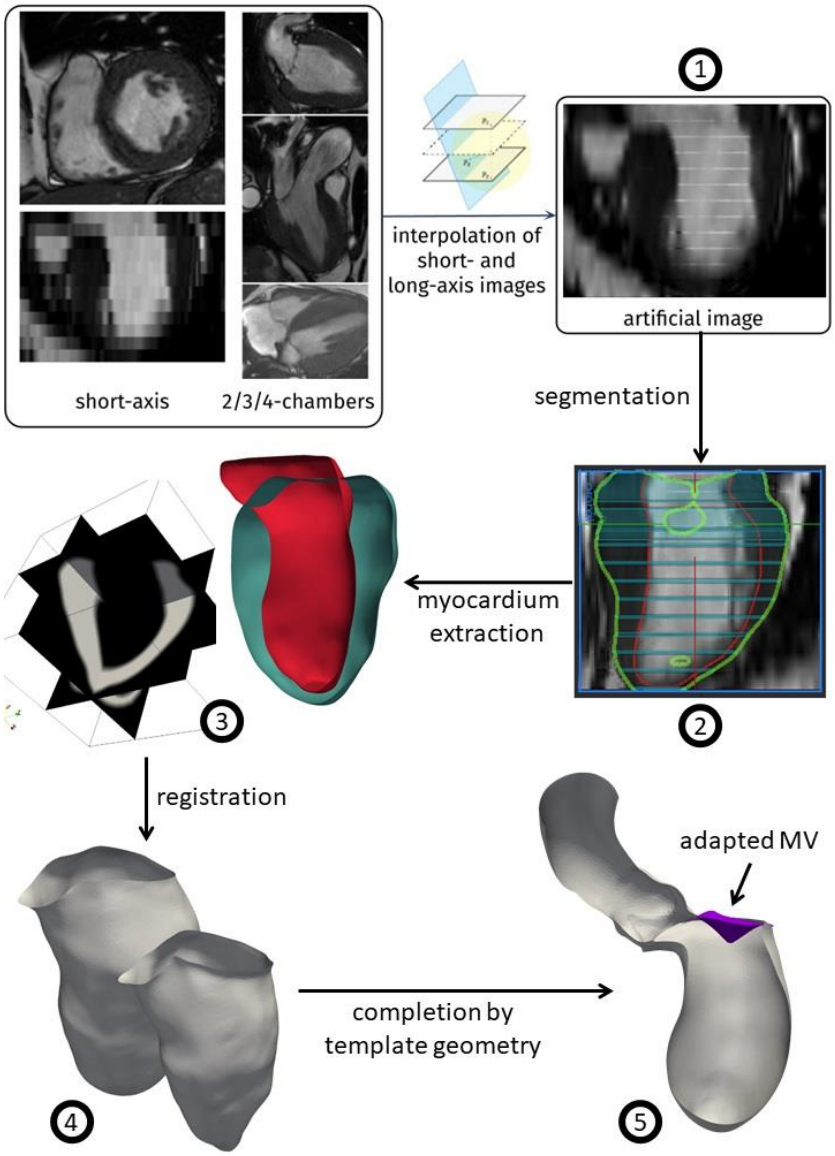

Figure 1 - Reconstruction algorithm. Numbers correspond to the steps of Algorithm 1.

Since the only available three-dimensional data was represented by the short-axis views, which however has a relatively low resolution along the LV main axis, we developed an algorithm to enhance the short-axis images with the long-axis acquisitions (commonly named as 2/3/4-chambers views) obtaining an artificial, time-dependent series of volumetric images with a uniform space resolution of 1mm in all directions. This represents the first step of our reconstruction algorithm, described in the following Algorithm 1 and depicted in Figure 1.

Algorithm 1 – Reconstruction procedure.

1. create an artificial image merging the information coming from all the different acquisition views: for each pixel laying between two short-axis acquisition planes, the grey-scale value of the artificial image is given by the average of nearby short-axis and long-axis values;
2. for each instant of the artificial image, segment both the endocardium and the epicardium of the LV;
3. intersecting the endocardium and epicardium surfaces obtained at the previous step, obtain a volumetric representation of the myocardium as a level-set image;
4. choosing the end of systole as a reference configuration, apply a registration algorithm among the level-set images of the myocardium, to obtain a displacement field for each acquisition time. The displacement field is applied to the endocardium surface of the reference configuration to obtain its evolution throughout the heartbeat;
5. complete the geometry resorting to a template geometry: from the Zygote solid 3D heart model [Zygote Media Group, Inc. 2014], a healthy heart complete geometry reconstructed from CT-scans, we extract the aorta and the mitral valve leaflets. The templates are adapted to the patient-specific LV, based on its aortic and mitral valves annulus, to obtain a complete computational domain for the study of the systolic phase, and the displacement field obtained in step 4 is extended to the whole geometry.

The reconstruction procedure presented above is an extension of the one we previously reported [Fumagalli et al. 2020]. The main advancement is represented by the generation of the enriched artificial images described at step 1 and their employment to accurately capture the patient-specific aorto-mitral annulus (exploited at steps 3 and 5) and the shortening and elongation of the LV directly from segmentation, without the need to measure it separately. The merging tools presented in the first step of the algorithm have been implemented in MATLAB (RRID:SCR_001622). As reconstruction tools, we employed the Medical Image Toolkit (MITK)[1] [Wolf et al. 2005, Nolden et al. 2013] for the segmentation step 2, a procedure based on SimpleITK[2] for the registration step 4, whereas for the other steps and for the automatic generation of the hexahedral mesh we employed the tools presented in [Fedele and Quarteroni, 2021] and other ad hoc semi-automatic tools hinging upon the Visualization Toolkit (VTK, RRID:SCR_015013)[3] and the Vascular Modeling Toolkit (VMTK, RRID:SCR_001893)[4] [Antiga et al. 2008]. Further details on this image-processing and surface-morphing procedure may be found in another report [Fumagalli et al. 2021].

Regarding the mitral valve, the use of a template geometry was motivated by the fact that, usually, standard MRI acquisitions do not provide sufficient details to allow an accurate reconstruction of the valves leaflets. Since we only investigated the systolic phase, and since mitral regurgitation was not present in any of the patients, the valve was maintained closed during the whole systolic phase. However, we believe it was important to include the mitral valve in the domain, since it defines two thirds of the LVOT boundaries and thus influences the blood dynamics, especially in a situation where it is displaced during the ventricular contraction (e.g., in SAM).

[1] www.mitk.org

[2] simpleitk.org

[3] www.vtk.org

[4] www.vmtk.org

2.3 Mathematical model – computational fluid dynamics

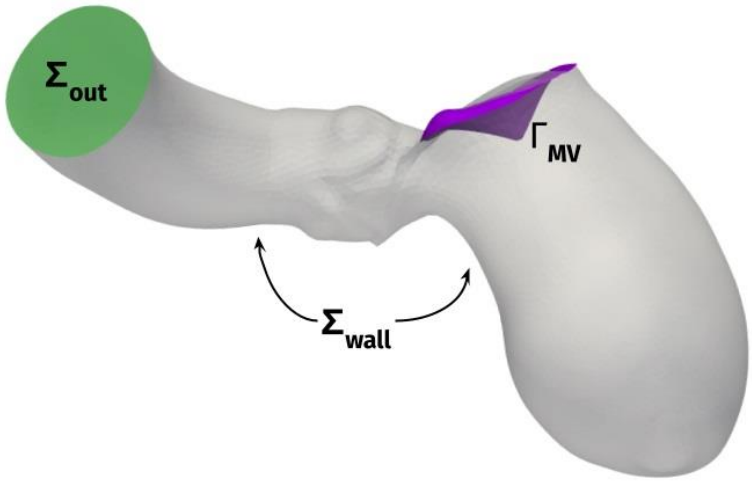

Figure 2 - Computational domain and mitral valve leaflets.

The computational domain, comprising the LV, the ascending aorta, and the surface Γ_{MV} representing the mitral valve leaflets, is displayed in Figure 2. Under the common assumption that blood is an incompressible Newtonian fluid, at least in the heart chambers and large vessels, we could model its flow by incompressible Navier-Stokes equations, with density $\rho = 1.06 \cdot 10^3$ kg/m3 and viscosity $\mu = 3.5 \cdot 10^{-3}$ Pa · s [Quarteroni et al. 2019]. An Arbitrary Lagrangian-Eulerian (ALE) formulation of the equations [Donea et al. 1982, Formaggia and Nobile 1999], allowed to prescribe the ventricular displacement reconstructed from images and extended to the whole wall Σ_{wall} as described in the previous section, whereas the effects of the mitral valve Γ on the flow were accounted for by the Resistive Immersed Implicit Surface (RIIS) method. RIIS lays in the class of immersed boundary methods [Peskin 1972, Iaccarino and Verzicco 2003, Mittal and Iaccarino 2005, Borazjani 2013, De Hart et al. 2003, van Loon et al. 2006, Griffith et al. 2009, Borazjani et al. 2010, Griffith 2012, Kamensky et al. 2015, Wu et al. 2018]. It was previously introduced by us [Fedele et al. 2017], based on the Resistive Immersed Surface method developed by another group [Fernández et al. 2008, Astorino et al. 2012], and it has been already applied by us in the study of the Systolic Anterior Motion (SAM) of the mitral valve [Fumagalli et al. 2020]. A comprehensive discussion on the numerical modeling of heart valves is available in the literature [Quarteroni et al. 2019, Mittal et al. 2016, Yoganathan et al. 2005, Sotiropoulos and Borazjani 2009, Votta et al. 2012, Marom 2015]. Since we focused our study on the systolic phase and none of the patients under investigation presented anomalies in their systemic pressure, we prescribed a physiological pressure waveform, derived from Wiggers diagrams [Wiggers 1923], as outflow condition at the distal section Σ_{out} of the ascending aorta. Because of the same reason, and as the main focus of the study was the assessment of the intraventricular obstruction, we did not include the aortic valve in the computational model.

The problem was numerically solved by means of a first order semi-implicit time discretization and a SUPG/PSPG-stabilized piecewise linear Finite Element Method for space discretization of both velocity and pressure (see [Fumagalli et al. 2020, Tezduyar and Sathe 2003, Bazilevs et al. 2007, Forti and Dedè 2015] for further details), implemented in life^{x} [5], a multiphysics high-performance

[5] gitlab.com/lifex

library based on the deal.II core[6] and developed in the iHEART project[7]. For all the patients, we discretized the domain by a hexahedral computational mesh with an average size of h = 1mm and a local refinement to h = 0.3mm in the region of the mitral valve and the LVOT, as shown in Figure 3. A simulation timestep of $\Delta t=10^{-4}$ s is adopted, and a smooth spline interpolation was used to represent the reconstructed displacements on the simulations time grid. We performed a mesh convergence test ensuring that no significant differences may be found by using a finer mesh or a smaller timestep.

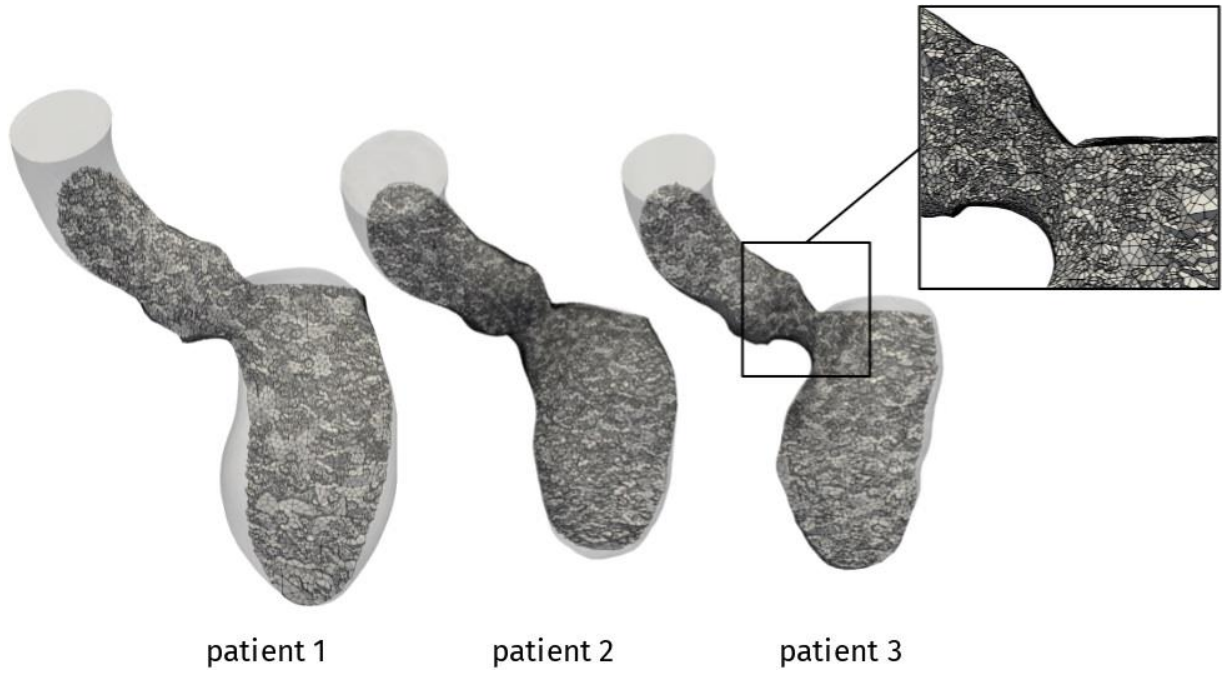

Figure 3 - Computational mesh for the patients under investigation. In the box, a zoom on the LVOT.

2.4 Outputs of interest

The reconstruction procedure and the computational methods described above allowed to obtain different relevant outputs about the overall cardiac function and the hemodynamics of the patients under investigation. In addition to well-known biomarkers such as the stroke volume (SV), the end-diastolic/end-systolic volume (ESV/EDV) and ejection fraction (EV), an accurate reconstruction of the LV volume changes occurring throughout the heartbeat was recovered. Then, focusing on the systolic phase, we could assess the possible HCM-induced obstruction in terms of velocity distribution, aortic jet development and pressure gradients. A particularly relevant indicator for the clinical assessment of the obstruction severity is the distribution of pressure along the septum. This information provides a quantitative measure of the spatial location and extension of the obstruction, very useful for the design of the surgical approach for HOCM: septal myectomy. Finally, thanks to the additional functionality offered by CFD with respect to diagnostical tests, we analyzed the Wall Shear Stress (WSS) on the endocardium and the aortic wall, which affects wall cell growth and

[6] www.dealii.org

[7] iHEART - An Integrated Heart model for the simulation of the cardiac function. European Research Council (ERC) grant agreement No 740132, P.I. Prof A. Quarteroni.

possible flow-induced damage [Dolan et al. 2013], and evaluated the turbulent and vortex structures developing in the aorta by the Q-criterion [Hunt et al. 1988].

3 Results

In this section, we present the outcomes of the proposed computational procedure for the data of three patients described above, in terms of geometrical, functional, and hemodynamics indicators.

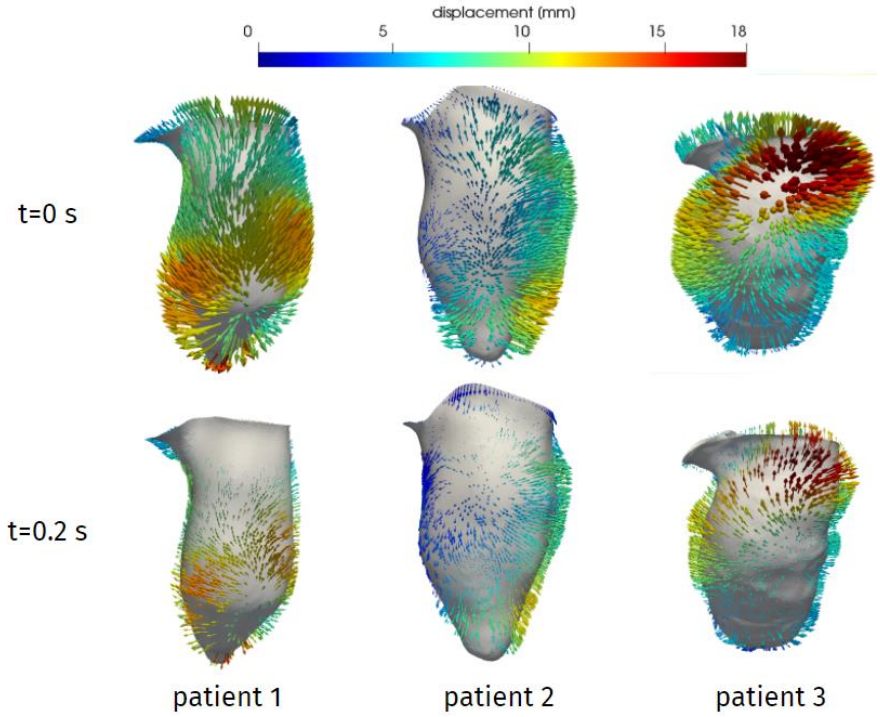

Figure 4 - Reconstructed displacement field of the three patients, at the end of diastole (t=0s) and in late systole (t=0.2s). LV aligned vertically, with septal wall on the left.

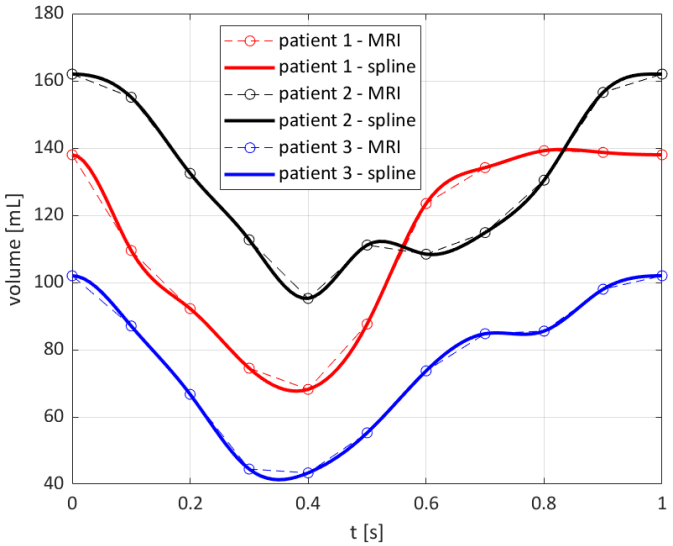

Figure 5 - Evolution of the reconstructed volume of the LV cavity.

Table 2 - End-diastolic volume (EDV), end-systolic volume (ESV) and ejection fraction (EF) as reconstructed from the computational procedure (above) and from clinical estimations (below).

PT	EDV [ml]	ESV [ml]	EF [%]
1	138	68	51
2	162	94	42
3	102	43	57
1	128	81	37
2	152	103	32
3	101	37	63

From the reconstruction procedure we obtained the displacement fields shown in Figure 4. The distribution of displacement and its intensity are significantly different among the three patients under investigation, expressing the high variability of the effects of HCM on the ventricular contractility. Indeed, we observe a generally reduced motion of the septal wall, and at the same time we can notice that for Patient 1 this reduction is mostly concentrated in the region near to the ventricular base, whereas Patient 2 has a more homogenously distributed hypokinesis. These differences in the movement of the endocardial wall are reflected in the evolution of the volume of the LV cavity (Figure 5). A remarkable difference in this sense is displayed by Patient 2, with a slowed diastolic expansion after the end of systole, at 0.4s. This is in accordance with the reduced ejection fraction of the patient (Table 2). In the same table, we can also compare the volume measurements obtained by our reconstruction with those estimated during the data acquisition. The end diastolic volumes (EDV) show a relatively good agreement between the reconstructed and estimated values, with a relative difference of less than 8% for all patients. On the other hand, the discrepancies between the two sources of data can be explained by the fact that the clinical estimates of volumes from cardiac cine-MRI are based on the approximation of LV as an ellipsoid [Hergan et al. 2008], which may not be particularly accurate for the end systolic volume (ESV), especially in the case of patients with HCM, for which contraction may be spatially inhomogeneous, and thus the geometry of the ventricle can present significant distortions.

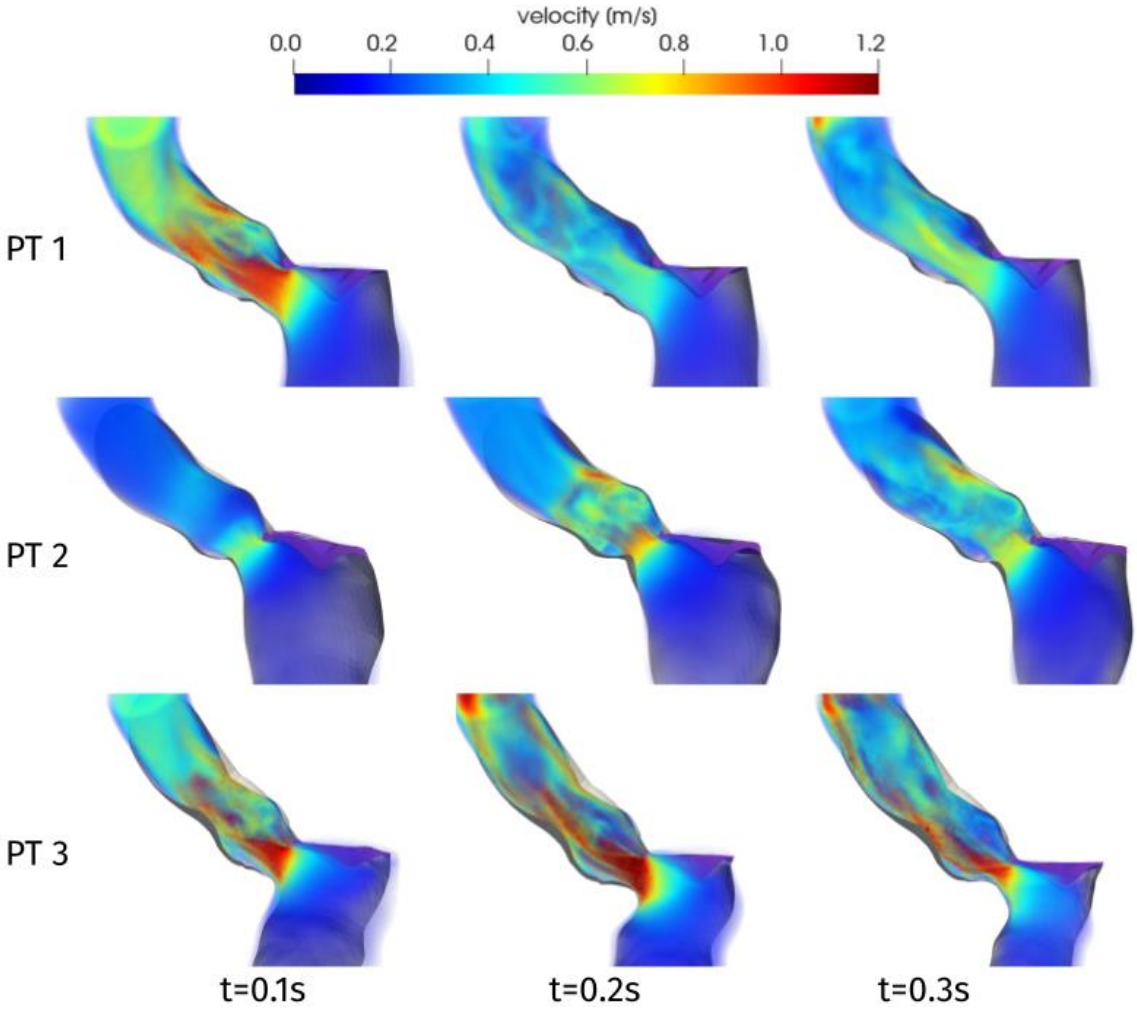

Figure 6 - Velocity distributions at significant times during systole.

Having discussed the reconstruction of the ventricular displacement, we now present the results of the computational hemodynamics simulations under such prescribed motion. As the aim of the present study was to assess the possible obstructions induced on the flow by HCM, we focus on the systolic phase. Figure 6 shows the blood velocity field for the three patients at three different times during the systolic phase. As a first aspect, we can notice significant differences in the timing of the systolic peak. Patient 1 shows a very quick blood acceleration in the early stages of the ejection, with a strong jet involving the whole aortic root and a maximum velocity of 1.38 m/s attained at t=0.08 s, then followed by a relatively slower deceleration. Patient 2 and 3, instead, present a more progressive development of the aortic jet, with a maximum velocity of 1.31 m/s and 2.2 m/s at times t=0.23s and 0.20 s, respectively, and persistent high velocity values (>1 m/s) also at later stages of the systolic phase. These two patients also have in common the impingement of the jet on the superior wall of the aorta, just downwind to the Valsalva sinuses, although with different velocity values. In terms of velocity peak, Patients 1 and 2 lay just above the limits of the range of physiological values (1-1.2 m/s), whereas Patient 3 attains a pathological value.

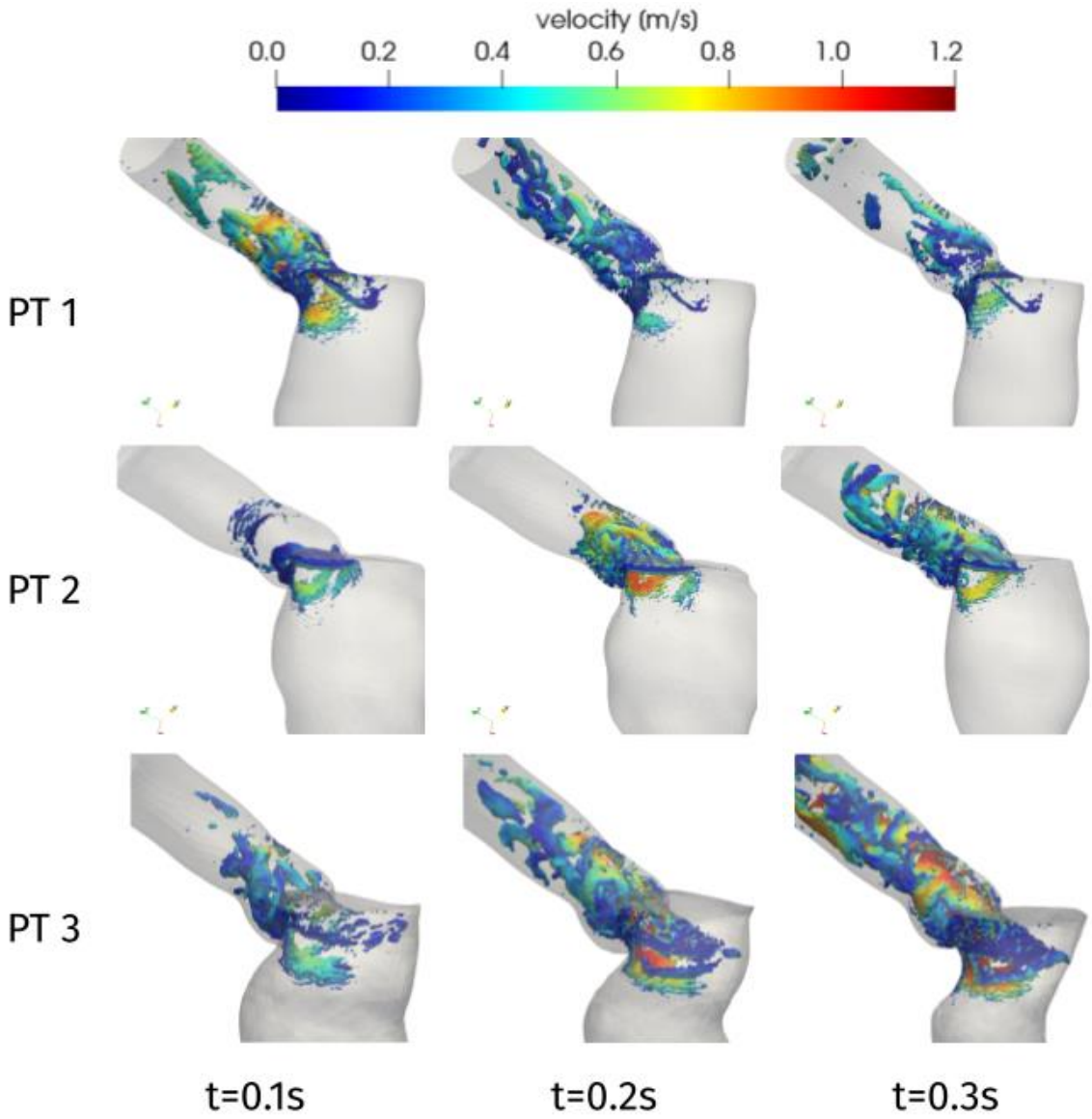

Figure 7 - Q-criterion contours (10 log-spaced values for Q in 2.4 · [10^4, 10^6] s^{-1}) colored by velocity magnitude at significant times during systole.

Further information on the blood flow can be obtained from the Q-criterion representation of Figure 7, which identifies vortex structures in the flow [Hunt et al. 1988]. In the case of Patient 1, coherent vortex structures form at the systolic peak (t=0.8s) in the aortic root, and then they are advected to the ascending aorta and dissipated during systole. For Patients 2 and 3, whose systolic peak occurs later (t=0.23s, t=0.2s, respectively), such structures develop progressively throughout systole, until the vortical flow that they represent interests the whole ascending aorta. Finally, the largest coherent structures are generated in the case of Patient 3: this is consistent with the high values of velocity magnitude reached in the LVOT and aortic root, that are typical of a flow in distinct transition to the turbulent regime (maximum Reynolds number in the aortic root: Re = 12000).

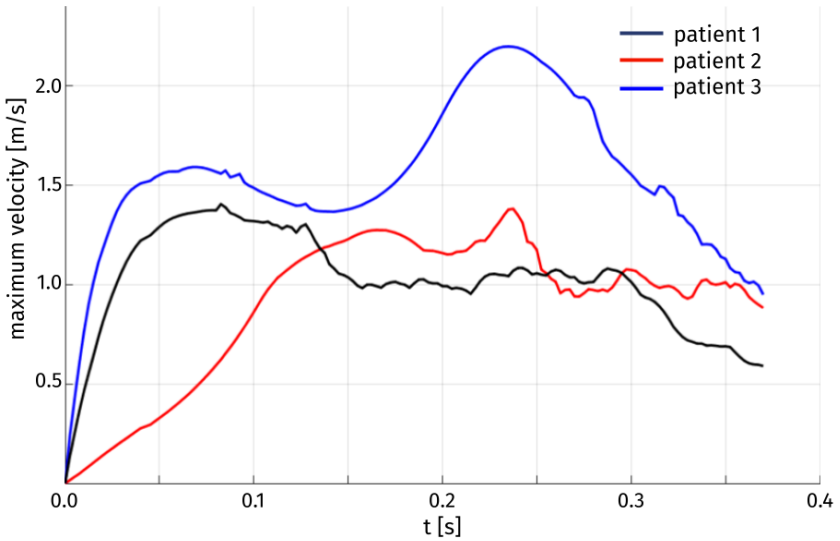

Figure 8 - Time evolution of the maximum blood velocity in the aorta.

Table 3 - Duration of the obstruction and threshold value for its identification.

PT	OBSTRUCTION DURATION [s]	THRESHOLD VALUE U_{thr} [m/s]
1	0.13	1.0
2	0.15	1.0
3	0.14	1.5

The velocity field can also be inspected to assess the *duration* of the HCM-induced obstruction. In particular, we consider the time evolution of the maximum blood velocity attained in the aorta, displayed in Figure 8, left: for all the three patients, we can notice that an interval of significantly higher velocity values is captured, whereas in the rest of the systolic phase the velocity shows little variations around a certain average value, that we denote by U_{thr}. Then, we can define the duration of the obstruction as the length of the largest time interval in which the maximum velocity remains above U_{thr}. The results are reported in Table 3. For the three patients, we can notice that the systolic obstruction occurs during about the 30% of the systole. This evaluation is particularly significant for Patient 3, which is the only one in which pathologically high peak velocity values are attained, as mentioned above. Similar considerations can be drawn from the evolution of the difference between the average pressure in the LV and in the Valsalva sinuses: a detailed analysis of the pressure gradient distribution is presented in the following.

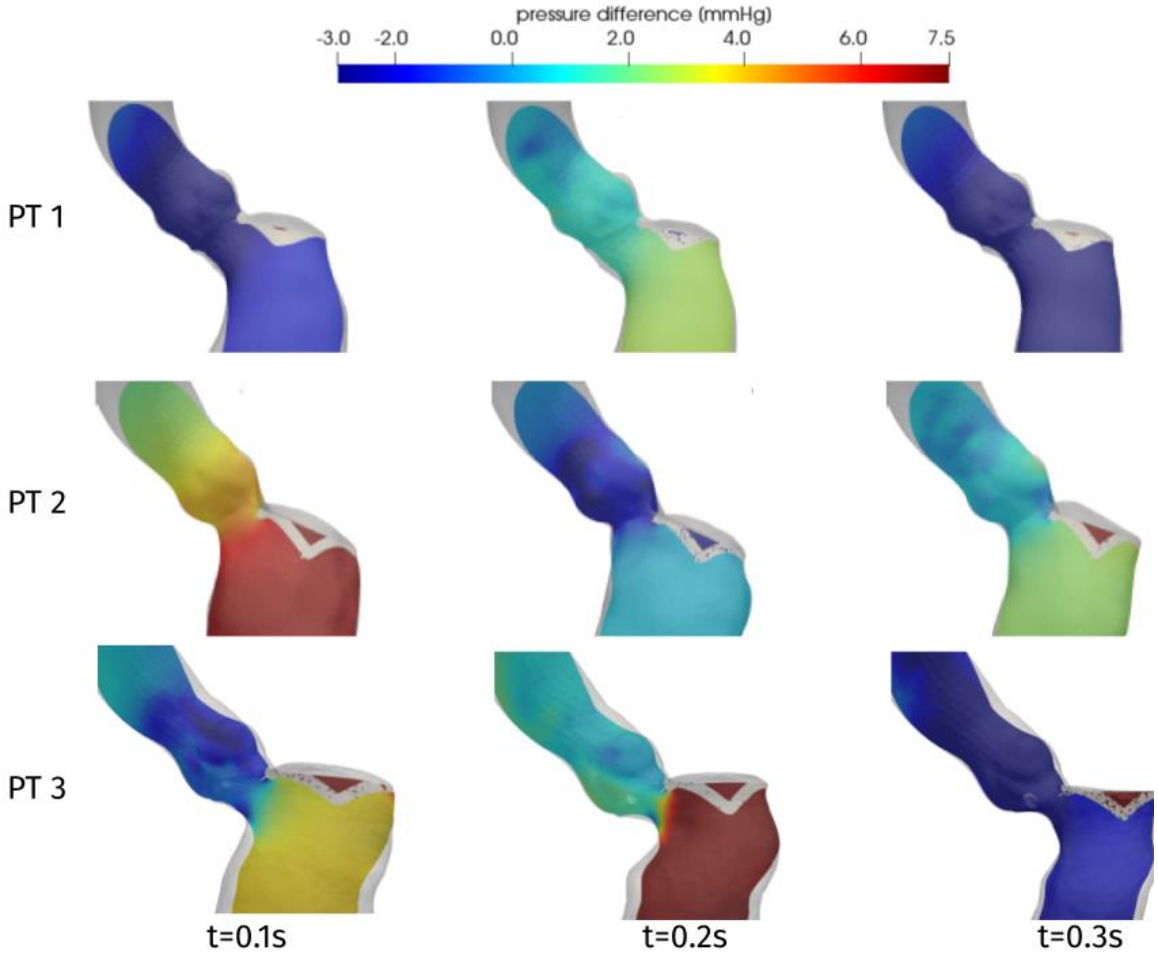

Figure 9 - Distribution of pressure difference $\Delta p = p\text{-}p_{AO}$ on a longitudinal slice, at significant times during systole.

One of the main quantities that is inspected in the assessment of the hypertrophy-induced obstruction is the intraventricular pressure gradient, that is the variation of pressure in the LVOT. Figure 9 displays the distribution of the difference $\Delta p = p\text{-}p_{AO}$ between the pressure p and its value p_{AO} in the center of Valsalva sinuses. For all patients and at all times, significant pressure gradients can be appreciated as expected in the LVOT and (at a smaller extent) in the Valsalva sinuses, whereas pressure is essentially uniform elsewhere. The overall pressure gradient of Patient 1 is always between -3 and 3 mmHg, whereas for the other two cases it is more than double. Regarding time evolution, each patient experiences an increase or a decrease of Δp at different stages of the systole, reflecting the variability that we observed above about the time dependence of the displacements and volume of the LV.

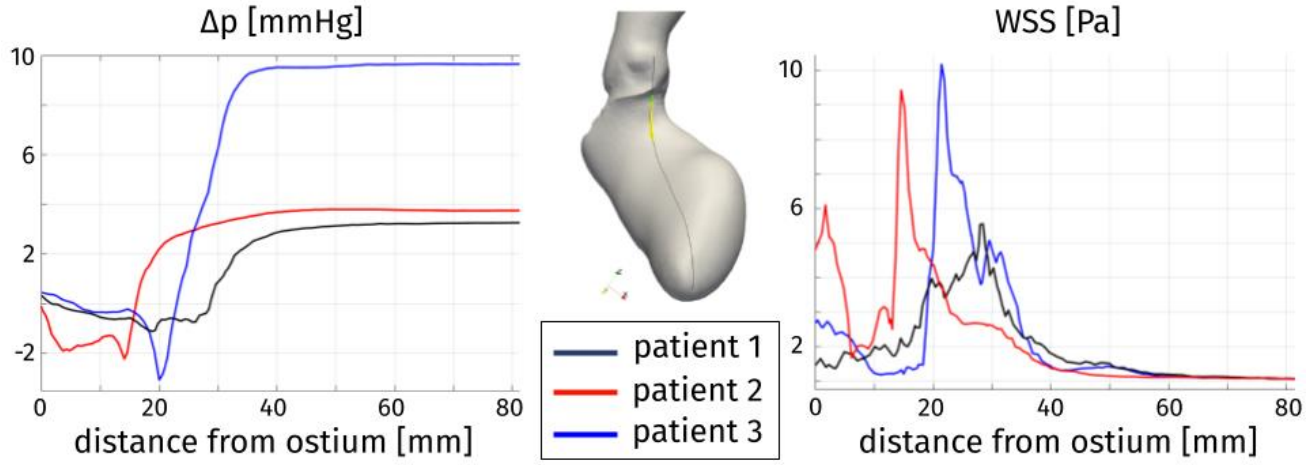

Figure 10 - Distribution of pressure difference with respect to the Valsalva sinuses (left) and wall shear stress (right) along a line on the septum (center), at the instant of maximum pressure gradient: Patient 1, t=0.08s; Patient 2, t=0.16s; Patient 3, t=0.20s.

In order to provide a synthetic evaluation of the severity of the hypertrophy-induced obstruction, and to quantify its localization and extension, Figure 10 displays a plot of the pressure difference Δp on a line running along the septum, from the right coronary sinus of Valsalva to the LV apex. Each of these curves refers to the time with the recording of the highest pressure gradient, for every patient. As a first comment, this plot confirms that the whole pressure gradient essentially develops in the LVOT and the aortic valve orifice. In particular, for each patient, the spatial position of the flow obstruction is identified by the sudden increase in pressure, that is notably significant for Patient 3, for which the interventricular gradient max(Δp)-min(Δp) = 12 mmHg is definitely larger than the typical physiological pressure difference between LV and ascending aorta (<5 mmHg, [Elliott et al. 2014]). In the case of Patient 3 we also observe a pressure drop concentrated in the subaortic portion of the LVOT.

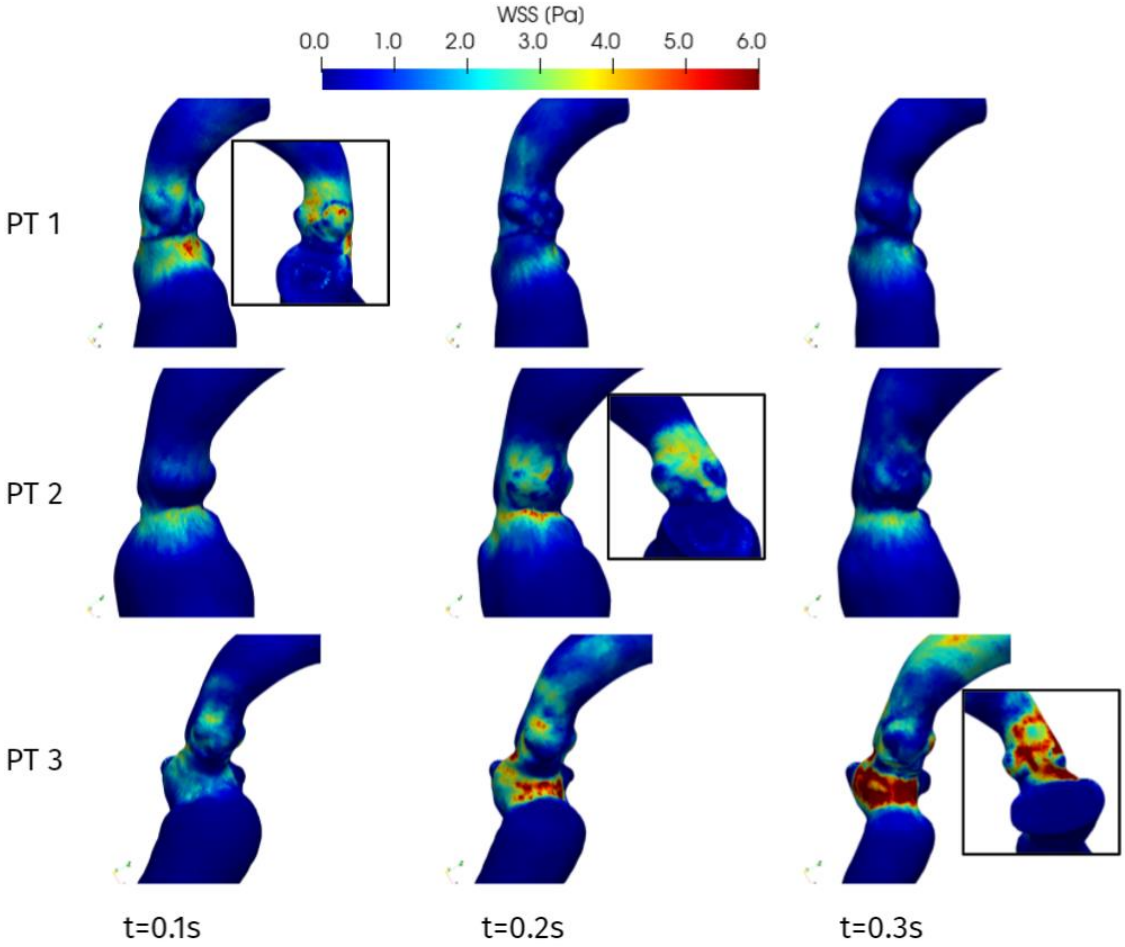

Figure 11 - Wall shear stress distributions at significant times during systole: view from the interventricular septum. In the boxes, WSS distribution on the aortic root wall at the systolic peak (view from the atrial side): Patient 1, t=0.08s; Patient 2, t=0.23s; Patient 3, t=0.20s.

Figure 11 represents the WSS distribution on the endocardium and aortic wall. The higher values of WSS are attained at the aortic root, particularly at the systolic peak, and at the septal wall of the LVOT, for all patients: in the first tract of the aorta these stresses are associated to the flow recirculation in the Valsalva sinuses, whereas in the LVOT they are due to the hypertrophic septum deviating the blood flow, consistently with the obstruction observed above in terms of velocity and pressure distribution. This is confirmed also by the line plot of Figure 10, where the WSS is shown to reach its maximum in correspondence of the maximum pressure gradient: within the LVOT region for Patients 1 and 3, at the aortic annulus for Patient 2. An interesting behavior is shown also by Patient 1: the WSS values remain nonnegligible on the septal part of the aortic annulus throughout the whole systole. Since such stresses are associated to velocity gradients, this is consistent with the persistent vortical structures that can be observed in Figure 7, in the same region.

4 Discussion

We introduced and applied an image-based computational approach for the analysis of the hemodynamics in patients suffering from hypertrophic cardiomyopathy. To reconstruct the geometry and the motion of the LV, we started from cine-MRI data, the gold standard for the clinical assessment of the heart function [Karamitsos et al. 2009, Gulsin et al. 2017, Maceira et al. 2006], especially regarding the diagnosis of HCM [Rickers et al. 2005, To et al. 2011, Maron 2012]. In particular, we

employed standard cardiac cine-MRI data routinely acquired in diagnostic procedures, without ad-hoc acquisition series, in order for our procedure to be applicable in virtually any clinical setting. From such data, we could generate a time-dependent, volumetric artificial image with a relatively high resolution in all directions, used to reconstruct the patient-specific geometry and motion of the left ventricle and ascending aorta during a complete heartbeat. The resulting time-dependent displacement was employed as a boundary condition for the computational fluid dynamics description of the blood flow, by Navier-Stokes equations in the ALE form. A resistive method was adopted to immerse the mitral valve leaflets in the domain.

The results of the reconstruction procedure displayed a considerable variability of the ventricle geometry and contractility among three different HCM patients. Different portions of the endocardium can be affected by hypokinesis, leading to different evolutions of the chamber volume and shape. The associated inhomogeneities in the ventricular displacement, as well as the assessment of the end-diastolic and end-systolic volume, showed how the ellipsoid approximation commonly employed in clinical evaluations may be quite inaccurate and yield a non-negligible underestimation of the ejection fraction.

In addition to the morphological data that can be extracted from clinical images, CFD simulations provide additional information on the blood flow in terms of velocity, vortical structures, and distribution of pressure and stress. To account for the domain motion, we adopted the approach of prescribed-motion CFD, which differs from the FSI approach in which the displacement of the cardiac muscle is the outcome of a mechanics model. By imposing directly the patient-specific image-based motion reconstructed from cardiac cine-MRI, we eliminated the need of a patient-dependent calibration of the myocardium mechanical model and the additional computational cost of solving the structural equations coupled with hemodynamics. This came at the expense of a more complex reconstruction procedure, described and discussed above. To the best of our knowledge, the present study represents the first comparison of the hemodynamics of HCM patients based on computational hemodynamics with image-based patient-specific endocardial displacement.

The hemodynamics results quantified the flow obstruction induced by the hypertrophy of the myocardium. For all the patients, the obstruction lasted for 30% of the duration of systole, thus for all of them further investigations and monitoring are advised. The typical systolic jet through the aortic orifice had significantly higher intensity in the case of obstruction than in the other cases, and this is strongly related with the pressure gradient developed in the LVOT and in the Valsalva sinuses.

The distribution of pressure on a line along the septum allowed to quantify the intraventricular pressure gradient and to identify its position and extension. The pressure increase occurs in a very short length, in the order of 10-15 mm, and its location is different among the patients: for Patient 2 the main obstacle to the flow is represented by the aortic annulus, whereas for Patients 1 and 3 the obstruction is within the LVOT. Therefore, for Patients 1 and 3 we can state that the obstruction is directly correlated with the HCM-induced thickening of the basal portion of the septum. Moreover, in Patient 3 a pressure drop concentrates in the subaortic portion of the LVOT: this accounts for the Venturi effect often acknowledged as the main cause of the SAM of the mitral valve, worsening the obstruction through the LVOT, as actually reported for this patient and previously discussed [Fumagalli et al. 2020].

From this assessment, we can also derive clinical indications useful in the design of the possible surgical treatment by septal myectomy. Although this procedure is well-established and typically entails low mortality and an impressive long-term survival rate [Ommen et al. 2005, Maron et al. 2014], it is currently designed combining the imaging data and the surgeon's experience, and more detailed

quantitative information may be useful. In this regard, our identification of the regions of high pressure gradient along the septum may be directly exploited during the surgical procedure, since the distances on the line that we draw, starting from the right coronary ostium and running towards the ventricular apex, can be measured on the surgical field.

Our analysis highlighted also other regions of the patients' anatomy that should be subject to follow-up examinations, although they are not directly involved by the hypertrophy. From the evaluation of the WSS, we could measure the impingement of the systolic jet on the aortic wall, particularly in the case of Patient 2 and 3, in whom follow-up future monitoring is advisable to reduce the risk of wall damage and possible aneurysm formation [Dolan et al. 2013].

4.1 Study limitations

First, the present study analyzed a small number of subjects, and none of them underwent surgery so far, based on the indications given by their attending clinicians. Therefore, our study represents a proof of concept, and for the moment ex-post clinical validation is still missing. However, being this a computational study, and not a statistical one, we designed an *a priori* model, supported by the imaging data and based on the physical principles of fluid-dynamics, and not an *a posteriori* model based only on clinical measurements. As a consequence, our sample is in fact not limited, and it allowed us to provide useful quantitative information about the patients, with the possibility of future utilization for other HCM patients. For sure, investigations involving a larger number of patients will achieve a more comprehensive understanding of the hemodynamics of HCM, confirming our preliminary results, and better accounting for the strong inter-patient variability of this clinical condition. To facilitate this process, an improved automatization of the reconstruction procedure is under development, to reduce the time elapsing between the acquisition of data and the post-processing of computational results.

Second, the aortic valve is not considered in the current settings, since, in the absence of pathological features, it is expected to have a negligible influence on the development of the intraventricular obstruction, which is the main feature of interest to classify HOCM. However, including also that valve in the geometry would allow an accurate assessment of the flow in the ascending aorta. To extend the assessment of the effects of HCM over the whole cardiac function, the model can be extended from the systolic phase to the full heartbeat (and possibly multiple heartbeats). This would entail to consider the valves opening and closing dynamics and to introduce a proper reconstruction of the left atrium: since such data is only partially available in standard cardiac cine-MRI data, an extension of the reconstruction algorithm should be envisaged.

Finally, alternative management options for HOCM, such as medical treatment with a combination of beta-blockers, calcium channel blockers, and/or antiarrhythmic medications, or other interventional approaches like septal ablation and potential implantation of cardioverter defibrillator, have not been discussed, as all of them are beyond the purpose of our computational study.

4.2 Conclusions

Regarding our patient population:

- The hypertrophy in Patient 1 does not induce an obstruction since little intraventricular pressure gradient is appreciable. Nevertheless, the inhomogeneous displacement partially hinders the effectiveness of the cardiac pump, with an ejection fraction that is just above the limit value of 50%.

- About Patient 2, the pressure gradient mainly develops at the aortic annulus, thus it is not directly associated to HCM. Moreover, it is of small magnitude, and it does not induce a pathologically intense aortic jet. However, the relatively large LV volume and rather generalized hypokinesis determine a low ejection fraction.
- Patient 3 fits different criterions for the definition of HOCM, with a strong aortic jet accompanied by a significant pressure gradient in the LVOT, and we could also quantify the Venturi effect that may have been at the origin of the development of a SAM of the mitral valve. Moreover, the obstruction has been localized, providing relevant indications for the design of a possible surgical treatment by septal myectomy.

These conclusions confirm the suitability and effectiveness of our proposed computational approach to assess the cardiac function and the hemodynamical implications of HCM, as well as to provide clinically relevant indications potentially useful to guide the surgical treatment of the disease.

5 Conflict of Interest

The authors declare that the research was conducted in the absence of any commercial or financial relationships that could be construed as a potential conflict of interest.

6 Author Contributions

IF: Conception of the study, development of the methods and software, image processing, simulations, analysis of the results, manuscript drafting, figures preparation, revision of manuscript. PV: Image processing, simulations, analysis of the results, figures preparation, revision of manuscript. CV: Conception of the study, analysis of the results, manuscript drafting, revision of manuscript, supervision of the study. MF: Development of the methods and software, revision of manuscript. AC: Clinical relevance of the results, revision of manuscript. SI: Images acquisition. RS: Clinical relevance of the results, revision of manuscript. AQ: Funding, Coordination of the study, Revision of manuscript.

7 Funding

This project has received funding from the European Research Council (ERC) under the European Union's Horizon 2020 research and innovation programme (grant agreement No 740132, IHEART 2017-2022, P.I. A. Quarteroni).

8 References

1. Elliott P, Anastasakis A, Borger M, Borggrefe M, Cecchi F, Charron P et al. ESC guidelines on diagnosis and management of hypertrophic cardiomyopathy: The task force for the diagnosis and management of hypertrophic cardiomyopathy of the European Society of Cardiology (ESC), *Eur Heart J* 35(39): 2733-2779, 2014.
   doi: 10.1093/eurheartj/ehu284.

2. Sherrid MV, Balaram S, Kim B, Axel L, Swistel DG. The Mitral Valve in Obstructive Hypertrophic Cardiomyopathy: A Test in Context. *J Am Coll Cardiol* 67(15): 1846-1858, 2016.
   doi: 10.1016/j.jacc.2016.01.071.

3. Akiyama K, Naito Y, Kinoshita M, Ishii M, Nakajima Y, Itatani K et al. Flow Energy Loss Evaluation in a Systolic Anterior Motion Case After the Ross Procedure. *J Cardiothorac Vasc Anesth* 31(6): 2118-2122, 2017.
doi: 10.1053/j.jvca.2017.03.006.

4. Geske JB, Cullen MW, Sorajja P, Ommen SR, Nishimura RA. Assessment of left ventricular outflow gradient: hypertrophic cardiomyopathy versus aortic valvular stenosis. *JACC Cardiovasc Interv* 5(6): 675-681, 2012.
doi: 10.1016/j.jcin.2012.01.026.

5. Ibrahim M, Rao C, Ashrafian H, Chaudhry U, Darzi A, Athanasiou T. Modern management of systolic anterior motion of the mitral valve. *Eur J Cardiothorac Surg* 41(6):1260-1270, 2012.
doi: 10.1093/ejcts/ezr232.

6. Jiang L, Levine RA, King ME, Weyman AE. An integrated mechanism for systolic anterior motion of the mitral valve in hypertrophic cardiomyopathy based on echocardiographic observations. *Am Heart J* 113(3): 633-644, 1987.
doi: 10.1016/0002-8703(87)90701-0.

7. Nicolò F, Lio A, Comisso M, Pantanella R, Scrofani R, Musumeci F. Surgical Treatment of Hypertrophic Obstructive Cardiomyopathy. In: *Cardiac Surgery Procedures*, edited by Montalto A, Loforte A, Amarelli C, IntechOpen, 2019.
doi: 10.5772/intechopen.86816.

8. Ommen SR, Maron BJ, Olivotto I, Maron MS, Cecchi F, Betocchi S, Gersh BJ et al. Long-term effects of surgical septal myectomy on survival in patients with obstructive hypertrophic cardiomyopathy. *J Am Coll Cardiol* 46(3): 470-476, 2005.
doi: 10.1016/j.jacc.2005.02.090.

9. Maron BJ, Nishimura RA. Surgical septal myectomy versus alcohol septal ablation: assessing the status of the controversy in 2014. *Circulation* 130(18): 1617-1624, 2014.
doi: 10.1161/CIRCULATIONAHA.114.011580.

10. Morrow AG, Reitz BA, Epstein SE, Henry WL, Conkle DM, Itscoitz SB et al. Operative treatment in hypertrophic subaortic stenosis. Techniques, and the results of pre and postoperative assessments in 83 patients. *Circulation* 52(1): 88-102, 1975.
doi: 10.1161/01.cir.52.1.88.

11. Quarteroni A, Manzoni A, Vergara C. The cardiovascular system: mathematical modelling, numerical algorithms and clinical applications. *Acta Numerica* 26: 365-590, 2017.
doi: 10.1017/S0962492917000046.

12. Kunzelman KS, Einstein DR, Cochran RP. Fluid-structure interaction models of the mitral valve: function in normal and pathological states. *Philos Trans R Soc Lond B Biol Sci* 362(1484): 1393-1406, 2007.
doi: 10.1098/rstb.2007.2123.

13. Su B, Zhong L, Wang XK, Zhang JM, Tan RS, Allen JC et al. Numerical simulation of patient-specific left ventricular model with both mitral and aortic valves by FSI approach.

Comput Methods Programs Biomed 113(2): 474-482, 2014.
doi: 10.1016/j.cmpb.2013.11.009.

14. Lassila T, Malossi C, Stevanella M, Votta E, Redaelli A, Deparis S. Simulation of left ventricle fluid dynamics with mitral regurgitation from magnetic resonance images with fictitious elastic structure regularization. arXiv:1707.03998 [physics.med-ph], 2017.

15. Feng L, Gao H, Griffith B, Niederer S, Luo X. Analysis of a coupled fluid-structure interaction model of the left atrium and mitral valve. *Int J Numer Method Biomed Eng* 35(11): e3254, 2019.
doi: 10.1002/cnm.3254.

16. Collia D, Vukicevic M, Meschini V, Zovatto L, Pedrizzetti G. Simplified mitral valve modeling for prospective clinical application of left ventricular fluid dynamics. *J Comp Phys* 398: 108895, 2019.
doi: 10.1016/j.jcp.2019.108895.

17. Kaiser AD, McQueen DM, Peskin CS. Modeling the mitral valve. *Int J Numer Method Biomed Eng* 35(11): e3240, 2019. (Corrigendum. Int J Numer Method Biomed Eng 36(9): e3349, 2020)
doi: 10.1002/cnm.3240.

18. Meschini V, Mittal R, Verzicco R. Systolic anterior motion in hypertrophic cardiomyopathy: a fluid–structure interaction computational model. *Theor Comput Fluid Dyn* 35: 381-396, 2021.
doi: 10.1007/s00162-021-00564-0.

19. Gao H, Feng L, Qi N, Berry C, Griffith BE, Luo X. A coupled mitral valve-left ventricle model with fluid-structure interaction. *Med Eng Phys* 47: 128-136, 2017.
doi: 10.1016/j.medengphy.2017.06.042.

20. Karabelas E, Gsell MAF, Augustin CM, Marx L, Neic A, Prassl AJ et al. Towards a Computational Framework for Modeling the Impact of Aortic Coarctations Upon Left Ventricular Load. *Front Physiol*. 9: 538, 2018.
doi: 10.3389/fphys.2018.00538.

21. Su B, Tan RS, Tan JL, Guo KWQ, Zhang JM, Leng S et al. Cardiac MRI based numerical modeling of left ventricular fluid dynamics with mitral valve incorporated. *J Biomech*. 49(7):1199-1205, 2016.
doi: 10.1016/j.jbiomech.2016.03.008.

22. D'Elia M, Mirabella L, Passerini T, Perego M, Piccinelli M, Vergara C et al. Applications of variational data assimilation in computational hemodynamics. In: *Modeling of Physiological Flows*, edited by Ambrosi D, Quarteroni A, Rozza G, Springer, 2011.
doi: 10.1007/978-88-470-1935-5_12.

23. This A, Morales HG, Bonnefous O, Fernández MA, Gerbeau J-F. A pipeline for image based intracardiac CFD modeling and application to the evaluation of the PISA method. *Comput Method Appl Mech Eng* 358: 112627, 2020.
doi: 10.1016/j.cma.2019.112627.

24. Otani T, Al-Issa A, Pourmorteza A, McVeigh ER, Wada S, Ashikaga H. A Computational Framework for Personalized Blood Flow Analysis in the Human Left Atrium. *Ann Biomed Eng* 44(11): 3284-3294, 2016.
doi: 10.1007/s10439-016-1590-x.

25. Chnafa C, Mendez S, Nicoud F. Image-Based Simulations Show Important Flow Fluctuations in a Normal Left Ventricle: What Could be the Implications? *Ann Biomed Eng* 44(11): 3346-3358, 2016.
doi: 10.1007/s10439-016-1614-6.

26. Seo JH, Vedula V, Abraham T, Lardo AC, Dawoud F, Luo H et al. Effect of the mitral valve on diastolic flow patterns. *Phys Fluids* 26(12): 121901, 2014.
doi: 10.1063/1.4904094.

27. Bavo AM, Pouch AM, Degroote J, Vierendeels J, Gorman JH, Gorman RC et al. Patient-specific CFD models for intraventricular flow analysis from 3D ultrasound imaging: Comparison of three clinical cases. *J Biomech* 50: 144-150, 2017.
doi: 10.1016/j.jbiomech.2016.11.039.

28. Deng L, Huang X, Yang C, Lyu B, Duan F, Tang D et al. Numerical simulation study on systolic anterior motion of the mitral valve in hypertrophic obstructive cardiomyopathy. *Int J Cardiol* 266: 167-173, 2018.
doi: 10.1016/j.ijcard.2018.01.062.

29. Nardi A, Bar G, Retzabi N, Firer M, Avrahami I. Hypertrophic Cardiomyopathy Treatment - A Numerical Study. In: *Computer Methods, Imaging and Visualization in Biomechanics and Biomedical Engineering. CMBBE 2019. Lecture Notes in Computational Vision and Biomechanics*, 36, edited by Ateshian G, Myers K, Tavares J, Springer, Cham, 2019.
doi: 10.1007/978-3-030-43195-2_3.

30. Fumagalli I, Fedele M, Vergara C, Dede' L, Ippolito S, Nicolò F et al. An image-based computational hemodynamics study of the Systolic Anterior Motion of the mitral valve. *Comput Biol Med* 123: 103922, 2020.
doi: 10.1016/j.compbiomed.2020.103922.

31. Fedele M, Faggiano E, Dedè L, Quarteroni A. A patient-specific aortic valve model based on moving resistive immersed implicit surfaces. *Biomech Model Mechanobiol* 16(5): 1779-1803, 2017.
doi: 10.1007/s10237-017-0919-1.

32. Zygote Media Group, Inc. Zygote Solid 3D Heart Generations I & II Development Report. *Technical Development of 3D Anatomical Systems*, 2014.

33. Wolf I, Vetter M, Wegner I, Böttger T, Nolden M, Schöbinger M et al. The medical imaging interaction toolkit. *Med Image Anal* 9(6): 594-604, 2005.
doi: 10.1016/j.media.2005.04.005.

34. Nolden M, Zelzer S, Seitel A, Wald D, Müller M, Franz AM et al. The Medical Imaging Interaction Toolkit: challenges and advances: 10 years of open-source development. *Int J*

Comput Assist Radiol Surg 8(4): 607-20, 2013.
doi: 10.1007/s11548-013-0840-8.

35. Fedele M, Quarteroni A. Polygonal surface processing and mesh generation tools for the numerical simulation of the cardiac function. *Int J Numer Method Biomed Eng* 37(4): e3435, 2021.
doi: 10.1002/cnm.3435.

36. Antiga L, Piccinelli M, Botti L, Ene-Iordache B, Remuzzi A, Steinman DA. An image-based modeling framework for patient-specific computational hemodynamics. *Med Biol Eng Comput* 46(11): 1097-1112, 2008.
doi: 10.1007/s11517-008-0420-1.

37. Fumagalli I, Fedele M, Pase G, Vergara C, Quarteroni A. An image-processing procedure for patient-specific cardiac hemodynamics. In preparation, 2021.

38. Quarteroni A, L. Dede', Manzoni A, Vergara C. Mathematical modelling of the human cardiovascular system: data, numerical approximation, clinical applications. Vol. 33. Cambridge University Press, 2019.

39. Donea J, Giuliani S, Halleux J-P. An arbitrary Lagrangian-Eulerian finite element method for transient dynamic fluid-structure interactions. *Comput Method Appl Mech Eng* 33 (1-3): 689-723, 1982.
doi: 10.1016/0045-7825(82)90128-1.

40. Formaggia L, Nobile F. A stability analysis for the arbitrary Lagrangian Eulerian formulation with finite elements. *East-West J Appl Math* 7(2): 105-131, 1999.

41. Peskin CS. Flow patterns around heart valves: A numerical method. *J Comp Phys* 10(2): 252-271, 1972.
doi: 10.1016/0021-9991(72)90065-4.

42. Iaccarino G, Verzicco R. Immersed boundary technique for turbulent flow simulations. *Appl Mech Rev* 56(3): 331-347, 2003.
doi: 10.1115/1.1563627.

43. Mittal R, Iaccarino G. Immersed boundary methods. *Annu Rev Fluid Mech* 37: 239-261, 2005.
doi: 10.1146/annurev.fluid.37.061903.175743.

44. Borazjani I. Fluid-structure interaction, immersed boundary-finite element method simulations of bio-prosthetic heart valves. *Comput Method Appl Mech Eng* 257: 103-116, 2013.
doi: 10.1016/j.cma.2013.01.010.

45. De Hart J, Peters GW, Schreurs PJ, Baaijens FP. A three-dimensional computational analysis of fluid-structure interaction in the aortic valve. *J Biomech* 36(1): 103-112, 2003.
doi: 10.1016/s0021-9290(02)00244-0.

46. van Loon R, Anderson PD, van de Vosse FN. A fluid-structure interaction method with solid-rigid contact for heart valve dynamics. *J Comp Phys* 217(2): 806-823, 2006. doi: 10.1016/j.jcp.2006.01.032.

47. Griffith BE, Luo X, McQueen DM, Peskin CS. Simulating the fluid dynamics of natural and prosthetic heart valves using the immersed boundary method. *Int J Appl Mech* 1(1): 137-177, 2009. doi: 10.1142/S1758825109000113.

48. Borazjani I, Ge L, Sotiropoulos F. High-resolution fluid-structure interaction simulations of flow through a bi-leaflet mechanical heart valve in an anatomic aorta. *Ann Biomed Eng* 38(2): 326-344, 2010. doi: 10.1007/s10439-009-9807-x.

49. Griffith BE. Immersed boundary model of aortic heart valve dynamics with physiological driving and loading conditions. *Int J Numer Method Biomed Eng* 28(3): 317-345, 2012. doi: 10.1002/cnm.1445. PMID: 25830200.

50. Kamensky D, Hsu MC, Schillinger D, Evans JA, Aggarwal A, Bazilevs Y et al. An immersogeometric variational framework for fluid-structure interaction: application to bioprosthetic heart valves. *Comput Methods Appl Mech Eng* 284: 1005-1053, 2015. doi: 10.1016/j.cma.2014.10.040.

51. Wu MCH, Zakerzadeh R, Kamensky D, Kiendl J, Sacks MS, Hsu MC. An anisotropic constitutive model for immersogeometric fluid-structure interaction analysis of bioprosthetic heart valves. *J Biomech* 74: 23-31, 2018. doi: 10.1016/j.jbiomech.2018.04.012.

52. Fernández M, Gerbeau J-F, Martin V. Numerical simulation of blood flows through a porous interface. *ESAIM-Math Model Num* 42(6): 961-990, 2008.

53. Astorino M, Hamers J, Shadden SC, Gerbeau J-F. A robust and efficient valve model based on resistive immersed surfaces. *Int J Numer Method Biomed Eng* 28(9): 937-959, 2012. doi: 10.1002/cnm.2474.

54. Mittal R, Seo J, Vedula V, Choi Y, Liu H, Huang H et al, Computational modeling of cardiac hemodynamics: Current status and future outlook. *J Comp Phys* 305: 1065-1082, 2016. doi: 10.1016/j.jcp.2015.11.022.

55. Yoganathan AP, Chandran KB, Sotiropoulos F. Flow in prosthetic heart valves: state-of-the-art and future directions. *Ann Biomed Eng* 33(12): 1689-1694, 2005. doi: 10.1007/s10439-005-8759-z.

56. Sotiropoulos F, Borazjani I. A review of state-of-the-art numerical methods for simulating flow through mechanical heart valves. *Med Biol Eng Comput* 47(3): 245-256, 2009. doi: 10.1007/s11517-009-0438-z.

57. Votta E, Le TB, Stevanella M, Fusini L, Caiani EG, Redaelli A et al. Toward patient-specific simulations of cardiac valves: state-of-the-art and future directions. *J Biomech* 46(2): 217-

228, 2012.
doi: 10.1016/j.jbiomech.2012.10.026.

58. Marom G. Numerical methods for fluid–structure interaction models of aortic valves», *Arch Comput Method E* 22(4): 595-620, 2015.
doi: 10.1007/s11831-014-9133-9.

59. Wiggers C. Modern aspects of the circulation in health and disease. Lea and Febiger, 1923.

60. Tezduyar T, Sathe S. Stabilization parameters in SUPG and PSPG formulations. *J Comp Appl Mech* 4(1): 71-88, 2003.

61. Bazilevs Y, Calo V, Cottrell J, Hughes T, Reali A, Scovazzi G. Variational multiscale residual-based turbulence modeling for large eddy simulation of incompressible flows. *Comput Meth Appl Mech Eng* 197(1-4): 173-201, 2007.
doi: 10.1016/j.cma.2007.07.016.

62. Forti D, Dedè L. Semi-implicit BDF time discretization of the Navier-Stokes equations with VMS-LES modeling in high performance computing framework. *Comput Fluids* 117: 168-18, 2015.
doi: 10.1016/j.compfluid.2015.05.011.

63. Dolan JM, Kolega J, Meng H. High wall shear stress and spatial gradients in vascular pathology: a review. *Ann Biomed Eng* 41(7): 1411-27, 2013.
doi: 10.1007/s10439-012-0695-0.

64. Hunt JCR, Wray AA, Moin P. Eddies, stream, and convergence zones in turbulent flows. Center for Turbulence Research Report, CTR-S88: 193-208, 1988.

65. Hergan K, Schuster A, Frühwald J, Mair M, Burger R, Töpker M. Comparison of left and right ventricular volume measurement using the Simpson's method and the area length method. *Eur J Radiol* 65(2): 270-278, 2008.
doi: 10.1016/j.ejrad.2007.03.031.

66. Karamitsos TD, Francis JM, Myerson S, Selvanayagam JB, Neubauer S. The role of cardiovascular magnetic resonance imaging in heart failure. *J Am Coll Cardiol* 54(15): 1407-1424, 2009.
doi: 10.1016/j.jacc.2009.04.094.

67. Gulsin GS, Singh A, McCann GP. Cardiovascular magnetic resonance in the evaluation of heart valve disease. *BMC Med Imaging* 17(1): 67, 2017.
doi: 10.1186/s12880-017-0238-0.

68. Maceira AM, Prasad SK, Khan M, Pennell DJ. Normalized left ventricular systolic and diastolic function by steady state free precession cardiovascular magnetic resonance. *J Cardiovasc Magn Reason* 8(3): 417-426, 2006.
doi: 10.1080/10976640600572889.

69. Rickers C, Wilke NM, Jerosch-Herold M, Casey SA, Panse P, Panse N et al. Utility of cardiac magnetic resonance imaging in the diagnosis of hypertrophic cardiomyopathy. *Circulation*

112(6): 855-861, 2005.
doi: 10.1161/CIRCULATIONAHA.104.507723.

70. To ACY, Dhillon A, Desai MY. Cardiac magnetic resonance in hypertrophic cardiomyopathy. *JACC-Cardiovasc Imag* 4(10): 1123-1137, 2011.
doi: 10.1016/j.jcmg.2011.06.022.

71. Maron MS. Clinical utility of cardiovascular magnetic resonance in hypertrophic cardiomyopathy. *J Cardiovasc Magn Reson* 14(1): 13, 2012.
doi: 10.1186/1532-429X-14-13.

MOX Technical Reports, last issues

Dipartimento di Matematica
Politecnico di Milano, Via Bonardi 9 - 20133 Milano (Italy)

28/2021 Ferro, N.; Perotto, S.; Bianchi, D.; Ferrante, R.; Mannisi, M.
Design of cellular materials for multiscale topology optimization: application to patient-specific orthopedic devices

26/2021 Vigano, L.; Sollini, M.; Ieva, F.; Fiz, F.; Torzilli, G.
Chemotherapy-Associated Liver Injuries: Unmet Needs and New Insights for Surgical Oncologists

27/2021 Scimone, R.; Menafoglio, A.; Sangalli, L.M.; Secchi, P.
A look at the spatio-temporal mortality patterns in Italy during the COVID-19 pandemic through the lens of mortality densities

25/2021 Tenderini, R.; Pagani, S.; Quarteroni, A.; Deparis S.
PDE-aware deep learning for inverse problems in cardiac electrophysiology

24/2021 Regazzoni, F.; Chapelle, D.; Moireau, P.
Combining Data Assimilation and Machine Learning to build data-driven models for unknown long time dynamics - Applications in cardiovascular modeling

22/2021 Domanin, M.; Bennati, L.; Vergara, C.; Bissacco, D.; Malloggi, C.; Silani, V.; Parati, G.; Trimarchi,
Fluid structure interaction analysis to stratify the behavior of different atheromatous carotid plaques

23/2021 Scimone, R.; Taormina, T.; Colosimo, B. M.; Grasso, M.; Menafoglio, A.; Secchi, P. *Statistical modeling and monitoring of geometrical deviations in complex shapes with application to Additive Manufacturing*

20/2021 Pasquale, A.; Ammar, A.; Falcó, A.; Perotto, S.; Cueto, E.; Duval, J.-L.; Chinesta, F.
A separated representation involving multiple time scales within the Proper Generalized Decomposition framework

21/2021 Torti, A.; Galvani, M.; Menafoglio, A.; Secchi, P.; Vantini S.
A General Bi-clustering Algorithm for Hilbert Data: Analysis of the Lombardy Railway Service

16/2021 Salvador, M.; Dede', L.; Manzoni, A.
Non intrusive reduced order modeling of parametrized PDEs by kernel POD and neural networks